Materials Science & Engineering A 748 (2019) 407–417

Contents lists available at ScienceDirect

Materials Science & Engineering A

journal homepage: www.elsevier.com/locate/msea

# Effects of additive manufacturing on the dynamic response of AlSi10Mg to laser shock loading

M. Laurençon[a,b], T. de Rességuier[a,*], D. Loison[c], J. Baillargeat[a], J.N. Domfang Ngnekou[a], Y. Nadot[a]

[a] Institut Pprime (UPR 3346), CNRS, ENSMA, Univ. Poitiers, 86961 Futuroscope, France
[b] Laboratoire MATEIS, INSA de Lyon, Université de Lyon 1, 69621 Villeurbanne, France
[c] Institut de Physique de Rennes, CNRS, Univ. Rennes 1, 35042 Rennes, France

ARTICLE INFO

*Keywords:*
AlSi10Mg
Selective Laser Melting
Laser shocks
Dynamic response
Spall fracture

ABSTRACT

In this study, the dynamic behaviour of light aluminum alloy AlSi10Mg obtained by additive manufacturing was investigated under laser shock loading. Two types of AlSi10Mg specimens were obtained by Selective Laser Melting (SLM) with two sets of building parameters, leading to specific architecture and microstructure compared to classical manufacturing processes. Their dynamic response to laser driven shocks was investigated on the basis of time-resolved measurements of free surface velocity, transverse visualization of shock-induced fragmentation, and post-recovery observations by means of microscopy. The results reveal a significant influence of the building parameters and SLM-inherited defects on both yield strength and spall strength values, as well as a strong dependence of high rate fracture behaviour on building direction of the material, mainly governed by melt pools shape and dissymmetry, with a combination of “interpool” and “intrapool” fracture modes.

## 1. Introduction

In the ongoing development of additive manufacturing (AM) processes, the characterization of physical properties and mechanical performances of the materials thus produced has become a key issue. Indeed, they offer many industrial possibilities by pushing back the technological locks linked to classical manufacturing processes. Among other things, they enable the design of geometrically complex engineering parts and offer new solutions for the most sophisticated applications, accounting for economic and ecological issues as they reduce tooling and loss of costly materials while saving energy. Several reviews summarized the concerns regarding additive manufacturing technologies [1–3]. The materials obtained by these new processes come with specific microstructure and unconventional mechanical behaviour. While their response to quasi-static loads has now been widely characterised, their dynamic behaviour, especially at very high strain rates, is still largely open to question.

Aluminum alloy AlSi10Mg is a hypoeutectic alloy widely used in transportation field and for aeronautical applications. Indeed, it constitutes a very attractive combination of lightness, good physical properties, mechanical performances, and ability to be processed. Moreover, this alloy is one of the rare aluminum alloys produced by AM nowadays, more particularly by Selective Laser Melting (SLM, also referred as Additive Layer Manufacturing). Thus, advanced work has been performed to characterise its properties inherited from AM process and investigate its mechanical behaviour under quasi-static loading [4–8]. However, very few studies have been reported yet on its dynamic behaviour, using Hopkinson bars or plate impacts, focusing on texture transition [9] or elastic-plastic response and spall fracture [10]. This latter work by Zaretsky et al. provided the yield strength (so called Hugoniot Elastic Limit, HEL) in compression as well as the dynamic tensile strength (so called spall strength) by measuring the free surface velocity profiles of impact-loaded AlSi10Mg targets obtained by SLM, compared to casted ones. Post-recovery fracture surfaces were observed by means of microscopy. The results reveal significantly higher dynamic properties for SLM alloy than for the one obtained by casting, as well as a ductile-brittle transition observed at strain rates comprised between $1\ s^{-1}$ and $5 \times 10^3\ s^{-1}$.

Among a variety of shock loading techniques, high power pulsed lasers provide access to very high strain rates and allow easy sample recovery for post-shock analysis (e.g. [11] and references therein), compared to more conventional techniques based on explosives or gas guns. High intensity irradiation of the target surface produces the ablation and vaporization of a thin layer of material into a plasma cloud

* Corresponding author.
*E-mail address:* thibaut.de-resseguier@ensma.fr (T. de Rességuier).

https://doi.org/10.1016/j.msea.2019.02.001
Received 10 December 2018; Received in revised form 31 January 2019; Accepted 1 February 2019
Available online 02 February 2019
0921-5093/ 

that expands in free directions thus driving a short compressive pulse in the sample. In this work, laser-driven shocks were generated in AlSi10Mg targets obtained by different SLM processes. Then their yield strength, spall strength, and fracture behaviour were correlated to microstructural features associated with AM.

## 2. Materials

### 2.1. Sample manufacturing

Samples were cut from 2 different productions of AlSi10Mg by SLM. The first bar, referenced as P1, was manufactured with a 400 W fiber laser, according to a meander laser scanning strategy in XY plan [12], with a scan speed of 1300 mm/s. The stack of layers was performed along the Z axis on a product support maintained at constant temperature of 200 °C, with a rotation of 67° between each layer of about 30 µm width. The second bar, referenced as P2, was produced in intentionally degraded conditions, from a powder supplied by TLS Technik™ with a 350 W fiber laser, on a platform maintained constantly at 150 °C in order to minimise residual stresses. The scanning strategy followed a meander pattern at a scan speed of 930 mm/s. The layering was performed by rolling (instead of scraping for P1 production) with a rotation angle of 90° between each layer of 50 µm width. Both productions were submitted to stress relaxation heat treatments. P2 bars were heat treated during 1 h at 210 °C whereas P1 production was maintained at 300 °C during 2 h. At the end of these heat treatments, both productions respect the standard NF EN 1706:2010, exhibiting the same chemical composition given in Table 1 [13]. P2 production contains flaws in the form of pores that lead to 2.25% of porosity, while P1 bars are 0.89% porous. Specimens were cut as 15 × 15 × 1 mm plates for P2 material and as 1 mm-thick disks of 15 mm diameter for P1, using electrical discharge machining. Then, they were polished mechanically to reach thicknesses comprised between 400 µm and 950 µm.

### 2.2. Structure of the material

The material microstructure is largely governed by SLM parameters [6,7]. The main architectural entity inherited from SLM process is the melt pool (Fig. 1) that follows the laser track and results from atomic segregation during the melting and resolidification of adjacent segments within the powder bed. Due to multi-layering and complex heat transfers associated with SLM process, melt pools have a dissymmetric shape (Fig. 1). Indeed, melt pools formation and layering imply the remelting of neighbouring, already formed melt pools due to interpenetration and overlap. This leads to a pronounced dissymmetry with a convex contour opposite to the building direction (bottom contour along -Z in Fig. 1) and two concave contours in the +Z direction of layering (top contours in Fig. 1). Inside these melt pools, grains grow epitaxially from the fusion line towards the centre of the pools, due to temperature gradient during cooling, and are consequently strongly anisotropic. In some cases, grains can be extended over several melt pools as the stacking implies the remelting of adjacent zones previously solidified. The microstructure inside columnar grains reveals a very fine dendritic cellular network consisting of α-Al matrix surrounded by Al-Si eutectic phase [13,14]. Due to SLM process, the material may develop different defects mainly in the form of porosity. Among these, lacks of fusion (Fig. 1) are characterised by irregular-shaped cavities that can reach mm-sizes. They are generally located at melt pools boundaries and they usually result from a too high scan speed combined to a low laser intensity, a too elevated hatch spacing (distance between two adjacent laser paths), or even an inadequate scanning strategy [15,16]. More commonly, metallurgical porosity is homogeneously distributed in the material, its formation being favoured by the high temperature of manufacturing inside the melt pool and by the pre-existing porosity of the powder grains (from gas atomisation).

### 2.3. Determination of density and sound velocity

As will be recalled next, the shock response of materials involves their sound velocity and density. To determine the density, two methods were used. The first one consists in measuring the mass (with a precision of ± 0.1 mg) and specimen volume from accurate dimensions measured with a profilometer (of ± 0.1 µm precision). The second one is based on mercury pycnometry, where measurements (still within a ± 0.1 mg uncertainty) of the mass of the empty pycnometer $m_0$, the mass of the pycnometer filled with mercury $m_l$, the mass of the pycnometer with the specimen in it $m_s$ and the total mass with both mercury and the specimen $m_{sl}$ provide the specimen density $\rho_0$ as

$$\rho_0 = \frac{\rho_l(m_s - m_0)}{(m_l - m_0) - (m_{sl} - m_s)} \quad (1)$$

where $\rho_L = 13{,}540\ \mathrm{kg/m^3}$ is the density of mercury in the testing conditions.

The final density $\rho_0$ for both productions, reported in Table 2, was obtained by averaging five measurements, where standard deviation was 5 $\mathrm{kg/m^3}$ and 8 $\mathrm{kg/m^3}$ in P1 and P2 materials, respectively. The lower density and higher scatter in P2 are consistent with the degraded production conditions (see Section 2.2) leading to more flaws and porosity in the form of lack of fusion.

Longitudinal sound velocity $c_L$ was measured using the pulse-echo method [17], where the transit time of ultrasounds propagating through specimens of known thickness (ranging from 3.74 to 20.03 mm) was recorded within a 0.1 µs accuracy. Measurements in the P1 alloy exhibited a standard deviation of 70 m/s around a mean value of 6480 m/s, in good agreement with the 6710 m/s mean value reported by Zaretsky et al. [10] in a similar alloy of slightly higher density (2656 $\mathrm{kg/m^3}$). Unexpectedly, this measured velocity was found to be independent of sample orientation with respect to building direction, like also reported in ref. [10]. The $c_L$ values measured in P2 samples were much more scattered, with a large standard deviation of 530 m/s around a mean value of 4910 m/s. Such scatter is attributed to the presence of lacks of fusion (see Section 2.2) in this alloy of poorer quality. Their random distribution within such relatively large specimens is likely to affect the propagation of ultrasounds, even though their low volume proportion does not modify much the overall density compared to the P1 alloy.

Unfortunately, transverse sound velocities $c_T$ could not be extracted from too weak signals, so that the values of the bulk sound speed $c_b$ could not be determined from the pulse-echo measurements. Instead, they were roughly assumed to be 17.5% lower than $c_L$, as reported in ref. [10]. Results are presented in Table 2.

## 3. Experimental setup

Laser shock experiments have been performed in two different facilities. In both cases, a high power pulsed laser is focused on a spot of a few mm-diameter in the sample surface, which produces the ablation of a thin layer of material and the formation of a plasma cloud. Plasma

**Table 1**
Material composition (wt%) in NF EN 1706:2010 standard.

| Element | Al | Si | Fe | Mg | Mn | Ti | Zn | Cu, Ni, Pb, Sn |
|---|---|---|---|---|---|---|---|---|
| Proportion | Bal. | 9.0–11.0 | < 0.55 | 0.2–0.45 | < 0.45 | < 0.15 | < 0.1 | < 0.05 |

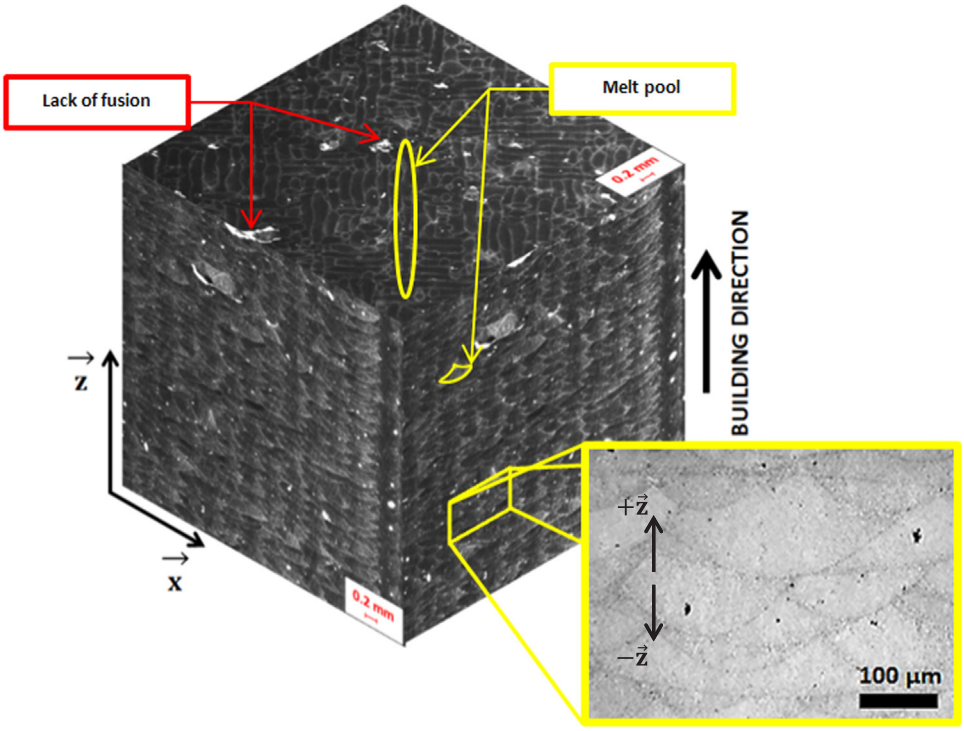


**Fig. 1.** 3D Reconstruction of optical micrographs showing the typical microstructure of SLM-produced AlSi10Mg alloy (after polishing, without etching). Melt pools are visible in their length on the top view, while the cube sides show them in their height (along the z axis) and width (along the x and y axes). The cube side length is 5.5 mm.

**Table 2**
Density and sound velocity of the AlSi10Mg alloys from SLM processes P1 and P2 (see text for details).

| Material | Density $\rho_0$ (kg/m$^3$) | Longitudinal sound velocity $c_L$ (m/s) | Bulk sound velocity $c_b$ (m/s) |
|---|---|---|---|
| P1 | 2646 | 6480 | 5345 |
| P2 | 2610 | 4910 | 4050 |

expansion towards the laser source drives, by reaction, a short compressive pulse which propagates from the irradiated spot into the metal. The velocity of the sample free surface, opposite to the loaded spot, is recorded with a Velocity Interferometer System for Any Reflector (VISAR) [18,19]. A continuous laser of 0.532 µm-wavelength is focused at the free surface of the sample. The Doppler shift due to the motion of that surface is used to produce interference fringes providing the surface velocity. As discussed elsewhere [11], the accuracy of this measurement is mainly limited by the uncertainty in the fringe count. With our push-pull type interferometer [19], this uncertainty was calculated to be less than ± 0.015 fringe [20], then reduced to ± 0.01 fringe [11] due to progress in electronics (photomultipliers and digitizing oscilloscope). The resulting error in the measured surface velocity is then ± 0.01/*F*, where *F* is the number of fringes or fringe fractions corresponding to this velocity [20].

A first set of low pressure shots was performed with a tabletop laser at Institut Pprime [21], delivering a pulse of 1.06 µm-wavelength, about 20 J-energy and 25 ns-duration focused on a spot of 4 mm-diameter. A water drop was put on top of the irradiated surface to confine the plasma expansion, in order to increase both the amplitude and the duration of the resulting pressure pulse [22], about 2.5 GPa and 50 ns, respectively. Such loading conditions allowed the investigation of the elastic-plastic behaviour of the alloy (Section 4.1). VISAR measurements were performed with a fringe factor of 0.542 km/s.

Higher pressure loads were needed to study spall fracture (Section 4.2). They were obtained in the LULI2000 facility of the Laboratoire pour l'Utilisation de Lasers Intenses (LULI, France), using a Nd: YAG laser pulse of 1.053 µm-wavelength, about 800 J-energy and 5 ns-duration focused on a 5 mm-diameter spot. To avoid laser breakdown in air at high intensity, samples were shot in secondary vacuum, which also prevented oxidation during shock-induced heating. In addition to the VISAR measurements of the free surface velocity (with a fringe factor of 1.895 km/s), transverse shadowgraphy was implemented to visualize fragmentation and debris ejection, using two ultra-fast cameras in alternate synchronisation (Fig. 2) providing one image every µs with an ultra-short exposure time of 5 ns to ensure minimum motion blur.

In order to study the effects of SLM process on the shock response of AlSi10Mg alloy, specimens were irradiated along their stacking direction (both +Z and -Z) and normally to this Z direction of layering (Fig. 3). Post-recovery specimens were observed using optical, Scanning Electronic Microscopy (SEM) and Field Emission Gun (FEG) microscopes. Observations were made on fracture surfaces and on cross sections after being coated in a resin and polished mechanically (without etching).

## 4. Results and discussion

As stated in Section 3, two sets of different laser shock experiments, involving shots of low and high intensity, were performed to study the elastic-plastic response to dynamic compression (Section 4.1) and the damage and fracture (spall) behaviour under high rate tensile loading (Section 4.2).

### 4.1. Hugoniot elastic limit

The main parameters of the low intensity shots are listed in Table 3. The corresponding VISAR records are presented in Fig. 4. After a transit time increasing with sample thickness, the first wave to emerge at the probed surface is called the elastic precursor which accelerates that surface to a velocity $2u_{HEL}$ of about 60 m/s (where $u_{HEL}$ is the particle velocity in the HEL state induced behind this elastic precursor). It is followed by a slightly slower plastic compression wave inducing a more progressive acceleration to the peak velocity, which decreases with sample thickness due to pressure decay with increasing propagation distance. Then, the free surface decelerates upon arrival of the

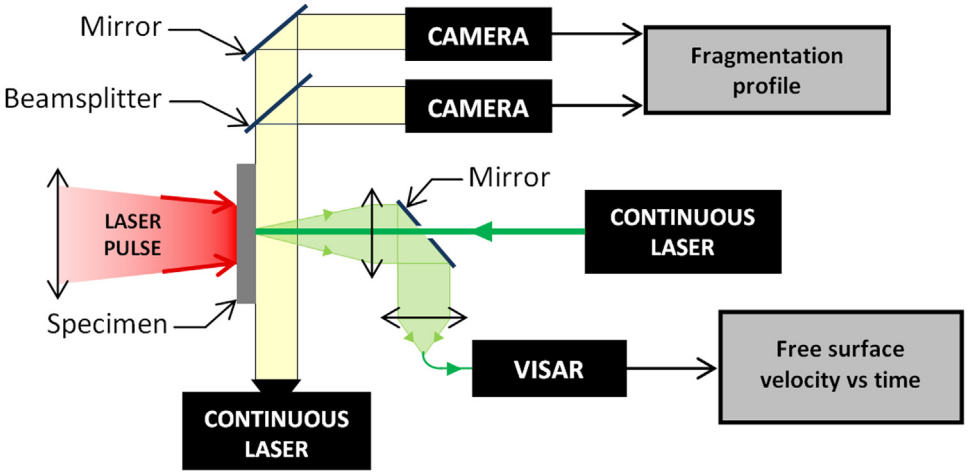


**Fig. 2.** Schematic of the LULI2000 laser shock experimental setup.

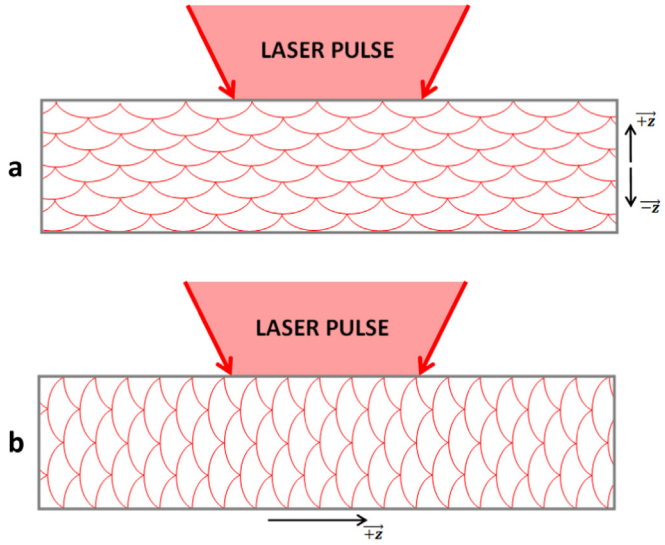


**Fig. 3.** Schematic of laser shock loading (a) along the stacking direction Z and (b) along a direction normal to the Z axis.

unloading wave, before a new acceleration after a "round trip" of the reflected wave back to the loaded surface then forth to the probed surface, with a reverberation period of about $2e/c_L$ here $e$ is the specimen thickness.

Based on free surface velocity profiles, the Hugoniot Elastic Limit $\sigma_{HEL}$ is derived from the particle velocity $u_{\mathrm{HEL}}$ behind the elastic precursor [23]:

$$\sigma_{HEL} = \rho_0 c_L u_{HEL} \quad (2)$$

Results are listed in Table 3 and plotted in Fig. 5. As stated in Section 3, the uncertainty in the VISAR measurement is less than $\pm 0.01/F$, where $F$ is typically 0.11 here (measuring $2u_{HEL}$ values of about 60 m/s with a fringe factor of 542 m/s), which leads to a ± 9% maximum error. As discussed in Section 2.3, further uncertainties in density and sound velocity values mainly arise from sample structure variability, especially in the P2 alloy. However, because the effects of such variability are expected to strongly depend on sample dimensions, the resulting errors seem difficult to quantify.

Overall, the HEL is observed to follow a decreasing trend with the increase of specimen thickness as classically observed in various materials (e.g. review in ref. [24]). Similar decay was reported in the same AlSi10Mg alloy under plate impacts [10], for a wider range of specimen thicknesses from 310 µm to 4.05 mm. Those impact-based values are in very good quantitative agreement with the velocities measured in our P1 specimens (Fig. 6), while results from the P2 specimens, where density and sound velocity are lower due to degraded manufacturing conditions, cannot be directly included in the comparison (see next).

P2 specimens present lower HEL values than denser P1 samples, at identical thicknesses and regardless of the direction of loading. Thus, the presence of pores, combined to detrimental building parameters, seems to lower the elastic limit of the material under dynamic compression, which is consistent with previous results in 25% porous tantalum specimens obtained by SLM and impacted by thick tantalum projectiles accelerated with a gas gun [25].

The HEL does not significantly depend on loading directions, as inferred from the similar values recorded in orthogonally loaded samples (P2-XY) and in those shocked along their Z stacking direction (P2-Z). This is in good agreement with results in ref. [10] that did not present any effect of the loading direction on HEL values. Nevertheless, the decay of the elastic precursor with propagation distance seems faster in samples loaded along the Z direction than normally to that

**Table 3**
Main experimental parameters and results for the low intensity shots shown in Fig. 4. The irradiated spot diameter is 4 mm and the pulse duration is about 25 ns.

| Specimen reference | Material | Sample thickness (µm) | Loading direction | Laser energy (J) | Laser intensity (GW/cm$^2$) | $2u_{HEL}$ (m/s) | Hugoniot elastic limit $\sigma_{HEL}$ (MPa) |
|---|---|---|---|---|---|---|---|
| P1-Z – 500 | P1 | 500 | Z | 17 | 7.87 | 63 | 540 |
| P1-Z – 600 | P1 | 600 | Z | 16 | 5.90 | 55 | 468 |
| P1-Z – 650 | P1 | 650 | -Z | 16 | 6.64 | 60 | 514 |
| P2-Z – 500 | P2 | 500 | Z | 16 | 6.61 | 65 | 416 |
| P2-Z – 600 | P2 | 600 | -Z | 16 | 6.06 | 65 | 416 |
| P2-Z – 700 | P2 | 700 | Z | 17 | 4.49 | 42 | 269 |
| P2-Z – 950 | P2 | 950 | +Z | 15 | 3.95 | 34 | 218 |
| P2-XY – 500 | P2 | 500 | ⊥Z | 16 | 6.13 | 66 | 423 |
| P2-XY – 600 | P2 | 600 | ⊥Z | 17 | 7.09 | 61 | 391 |
| P2-XY – 900 | P2 | 900 | ⊥Z | 18 | 6.27 | 61 | 391 |

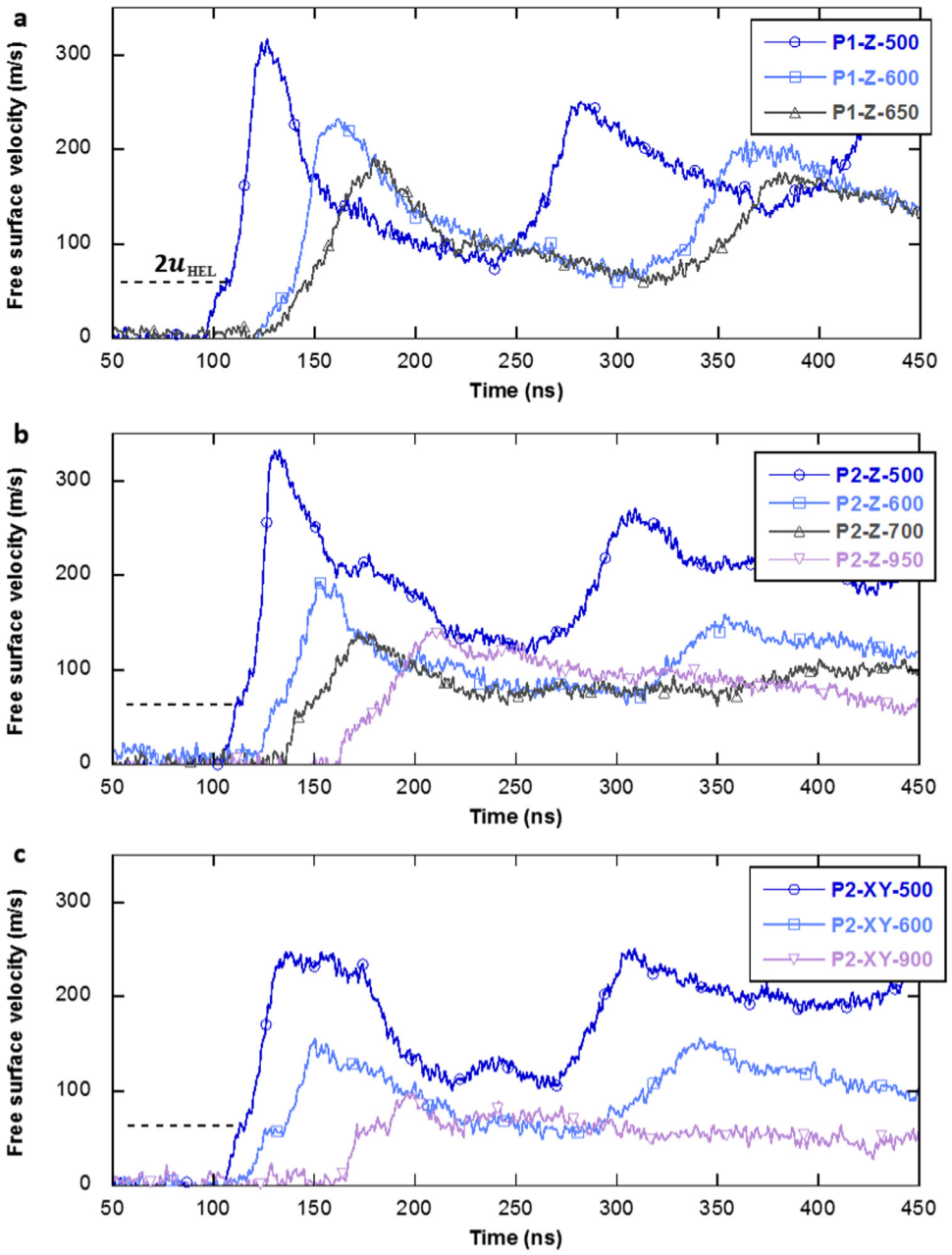


**Fig. 4.** Free surface velocity profiles recorded in (a) P1 samples loaded along Z axis, (b) P2 samples loaded along Z axis and (c) P2 samples loaded orthogonally to Z axis. Samples are referenced with their thickness in μm.

direction, leading to a significant gap in thick specimens (Fig. 5). If this decay is assumed to be enhanced by the presence of defects located preferentially at melt pools boundaries, such gap is qualitatively consistent with the number of these boundaries across a given thickness, higher in a Z-cut specimen (Fig. 3a) than in a XY-cut sample (Fig. 3b).

### 4.2. Spall fracture

Fig. 7 shows the free surface velocity profiles recorded in the high intensity laser experiments, corresponding to the parameters presented in Table 4. In this case of higher loading pressures, the elastic precursor is overdriven, i.e. the shock front (including both elastic and plastic compression), which propagates faster than $c_L$, does not split into two waves, so that the HEL cannot be determined from the records. On the other hand, unlike in Fig. 4, the deceleration from the peak velocity is interrupted by a reacceleration, followed by damping oscillations around a finite, approximately steady velocity, with no reloading after a "round trip" throughout the sample thickness. This is typical of spall fracture occurring inside the specimen, at some finite depth beneath the free surface (spall plane), where the interaction of the incident unloading wave with the rarefaction wave reflected from that surface induces tensile stresses [23]. When this local tension exceeds the dynamic tensile strength (spall strength) of the material, it is relaxed by crack opening, which produces a recompression wave. Subsequent reacceleration of the free surface is called the spall pulse, and the spall strength $\sigma_{spall}$ can be classically inferred from the amplitude $\Delta u_{fs}$ of the velocity pullback from the peak velocity to the spall pulse (see Fig. 7), using a common, so-called acoustic approximation [11,23]:

$$\sigma_{spall} = \frac{1}{2}\rho_0 c_b \Delta u_{fs} \tag{3}$$

The strain rate can be determined as

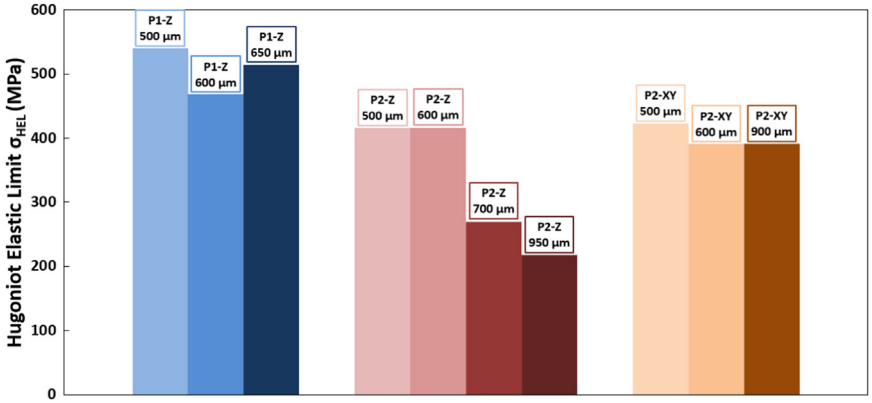


**Fig. 5.** Hugoniot Elastic Limit of laser shock-loaded AlSi10Mg produced by SLM. Material reference, loading direction and sample thickness in µm are indicated on each bar.

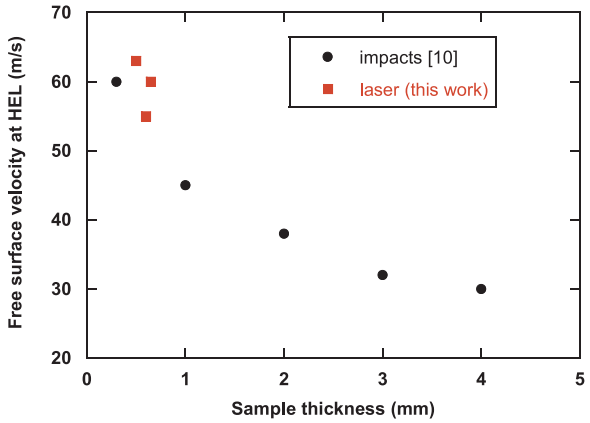


**Fig. 6.** Free surface velocity recorded upon breakout of the elastic wave in SLM-produced AlSi10Mg samples of increasing thickness subjected to laser shocks (red squares, this work, P1 alloy) or plate impacts (black circles, ref. [10]). Note that the plotted values (free surface velocity) are called $2u_{HEL}$ here instead of $u_{HEL}$ in ref. [10].

$$\dot{\varepsilon} = \frac{1}{2c_b}\frac{\Delta u_{fs}}{\Delta t} \tag{4}$$

where $\frac{\Delta u_{fs}}{\Delta t}$ is the rate of velocity decrease during the deceleration part of the records.

Again, the experimental uncertainty in the velocity is ± 0.01/*F*, where *F* is now about 0.14 (measuring $\Delta u_{fs}$ values of about 270 m/s with a fringe factor of 1895 m/s), which leads to a ± 7% maximum error. Again, additional uncertainties on density and sound velocity values, mostly due to sample structure variablility, are more difficult to estimate.

Measurements reveal significantly higher spall strengths for P1 specimens than for P2 specimens. This is consistent with the fact that, as previously reported in different materials [26,27], the resistance to spall damage usually decreases with increasing porosity. More generally, P2 specimens have been built in degraded conditions, with a larger stripe distance between two laser tracks in a same layer (50 µm) as well as a higher angle between laser track directions of successive layers (90° against 67°), which differences are likely to be detrimental to the material cohesion.

Spall strength appears to be almost identical for both directions of shock loading, either parallel or normal to the stacking direction Z. This is consistent with results for the same alloy under plate impacts [10], for which spall strengths are reported to be similar in both loading directions, about 1.75–1.80 GPa, in good quantitative agreement with the values measured in our P1 samples at slightly higher strain rates.

Fragmentation profiles obtained by transverse shadowgraphy are presented in Fig. 8, for P1 and P2 samples subjected to high pressure laser shocks. They show the formation and subsequent ejection in vacuum of one or several spalled layers followed by secondary fragments. Due to late breaking at the periphery of the loaded zone, under shear

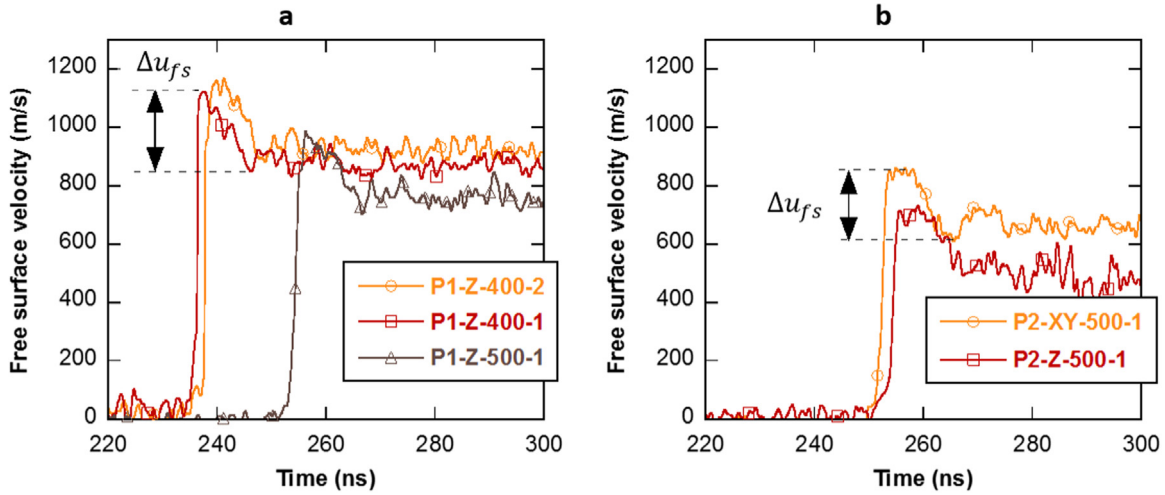


**Fig. 7.** Free surface velocity profiles recorded in (a) P1 samples, (b) P2 samples. Shots are referenced with the direction of shock application and sample thickness in µm.

**Table 4**
Main experimental parameters and results for the high intensity shots shown in Fig. 7. Laser pulse duration is 5 ns and the irradiated spot diameter is 5 mm.

| Specimen reference | Material | Sample thickness (μm) | Loading direction | Laser energy (J) | Laser intensity (GW/cm$^2$) | $\Delta u_{fs}$ (m/s) | $\sigma_{spall}$ (GPa) | $\dot{\varepsilon}$ ($10^6$ s$^{-1}$) |
|---|---|---|---|---|---|---|---|---|
| P1-Z-400–1 | P1 | 400 | +Z | 757 | 789 | 271 | 1.88 | 2.35 |
| P1-Z-400–2 | P1 | 400 | +Z | 702 | 735 | 277 | 1.92 | 3.30 |
| P1-Z-500–1 | P1 | 500 | -Z | 785 | 815 | 280 | 1.94 | 2.49 |
| P2-Z-500–1 | P2 | 500 | +Z | 696 | 713 | 239 | 1.24 | 2.01 |
| P2-XY-500–1 | P2 | 500 | ⊥ Z | 686 | 726 | 241 | 1.25 | 2.34 |

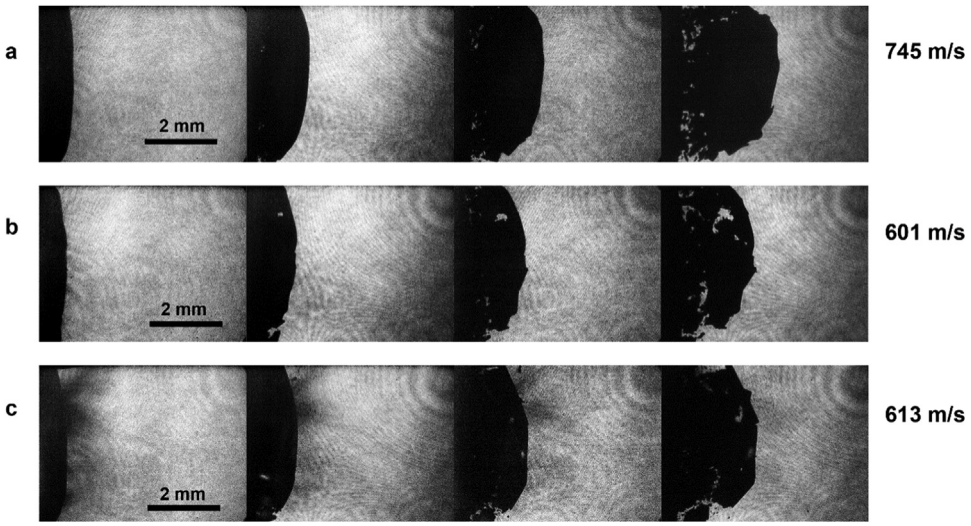


**Fig. 8.** Transverse shadowgraphs recorded at 1 μs, 2 μs, 3 μs and 4 μs from left to right, in (a) P1-Z, (b) P2-Z and (c) P2-XY samples, with the mean velocity of the main spalled layer indicated to the right of each sequence.

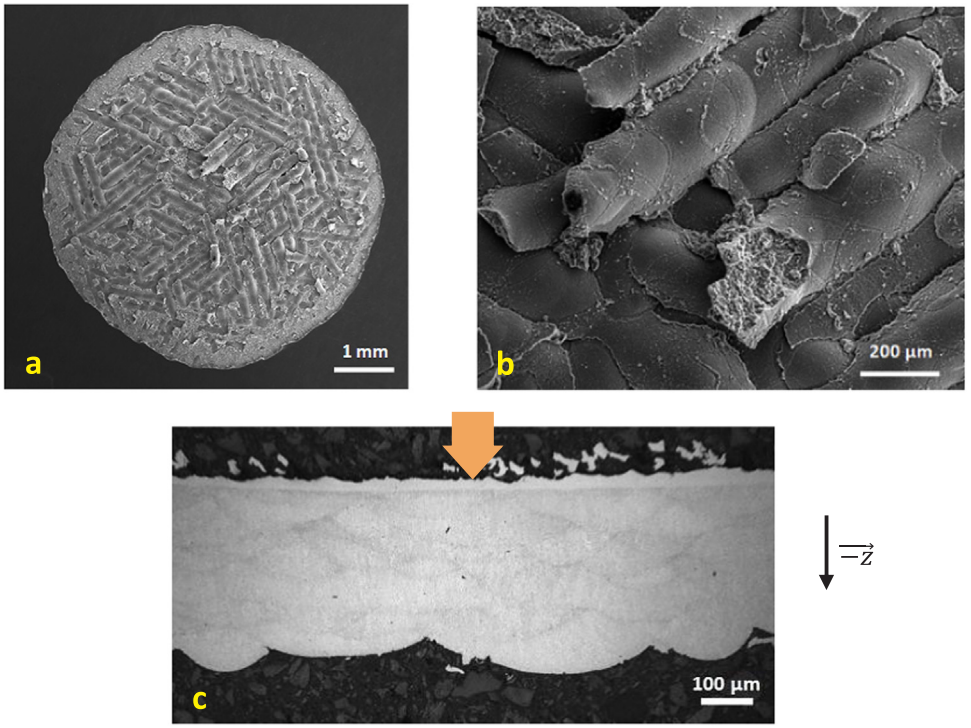


**Fig. 9.** Post-shot observations of sample P1-Z-500–1 shocked along the –Z axis: Scanning Electron Micrographs of the spall crater (a, b) and optical micrograph of a cross section (c).

and tensile stresses, the curvature of the free surface is seen to increase over the first μs. The position of the centre of the free surface is observed to increase linearly with time, which provides the mean (basically constant) flight velocity of the fastest fragments, given to the right of each sequence. Logically, these mean velocities are found to agree well with those measured at the end of the VISAR records of

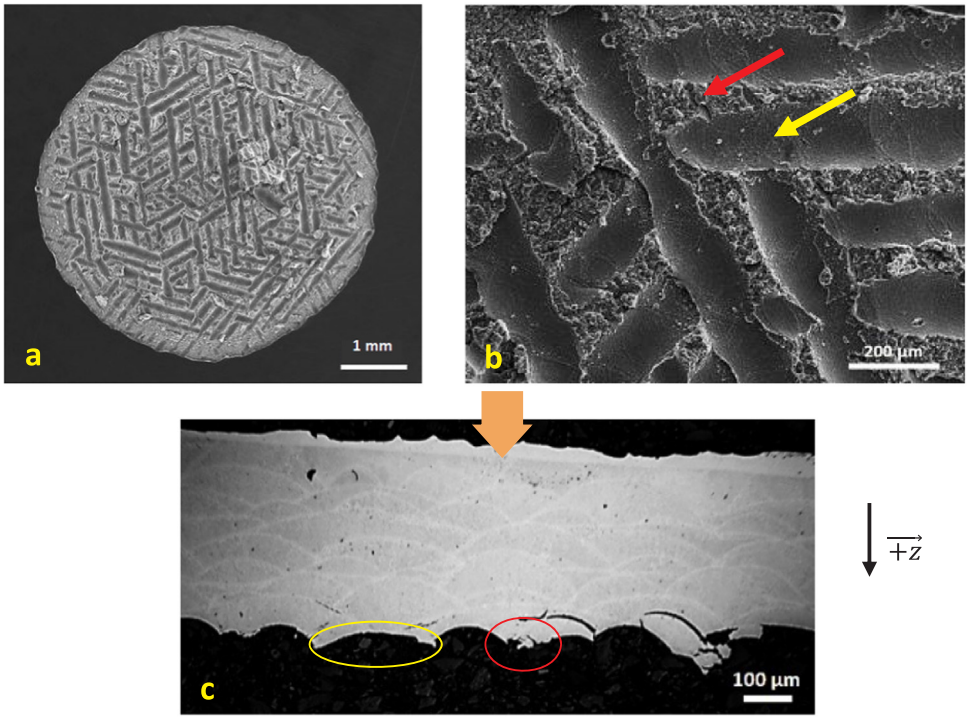


**Fig. 10.** Post-shot observations of sample P1-Z-500–2 shocked along the +Z axis: Scanning Electron Micrographs of the spall crater (a, b) and optical micrograph of a cross section (c). Arrows and circles show both intrapool (red) and interpool (yellow) fractures.

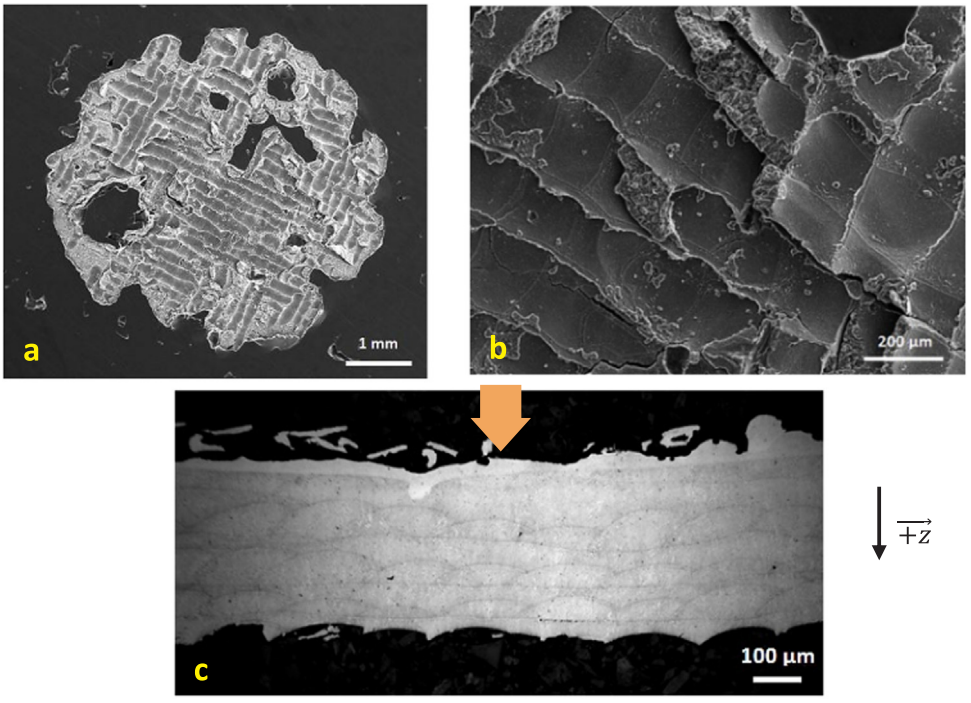


**Fig. 11.** Post-shot observations of sample P2-Z-500–1 shocked along the +Z axis: Scanning Electron Micrographs of the spall crater (a, b) and optical micrograph of a cross section (c).

Fig. 6, when free surface velocities reach a final, roughly constant value. They are significantly higher in the P1 specimen than in the P2 samples. This discrepancy is mainly attributed to the faster pressure decay during pulse propagation throughout more porous samples, leading to lower shock breakout pressures and lower free surface velocities. Fragmentation profiles seem smoother and more homogeneous in P1 (Fig. 8a) than in P2 samples (Fig. 8b and c), where more irregularities and sharp angle changes are observed. This suggests a more chaotic fragmentation in P2 material, as will be confirmed next by SEM images.

Microscopy observations of recovered specimens (Figs. 9–13) show spall craters in their free surface, both as front views (SEM) and cross sections (optical micrographs). Overall, the craters are very different in P1 and P2 materials. While they present very homogeneous and nicely circular contours in P1 samples (Fig. 9a and Fig. 10a), they are more chaotic in P2 specimens (Fig. 11a and Fig. 12a), which is consistent

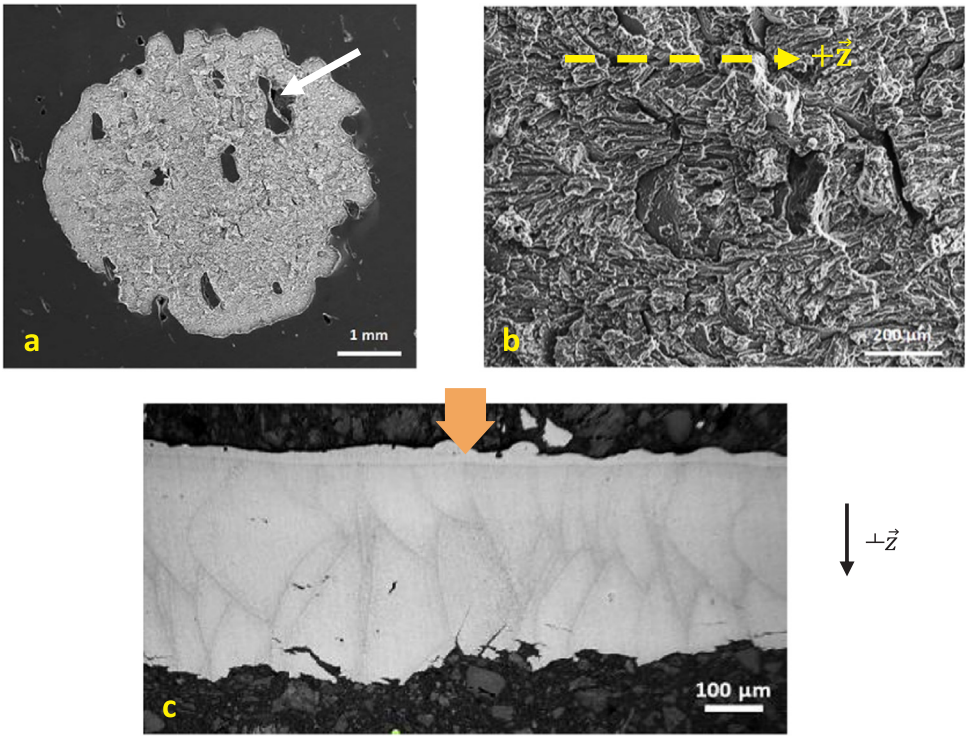


**Fig. 12.** Post-shot observations of sample P2-XY-500–1 shocked along the normal to the building direction: Scanning Electron Micrographs of the spall crater (a, b) and optical micrograph of a cross section (c). The white arrow points to a lack of fusion. Fracture is mainly intrapool, except for some interpool cracks at boundaries of propitious location and orientation.


**Fig. 13.** Optical micrograph of a cross section in sample P1-Z-500–1 shocked along the –Z axis (same as Fig. 9) at the edge of the loaded zone, where two distinct spalled layers have separated from the bulk. Shock loading has been applied from top to bottom (arrow).

with the fragmentation profiles above, with irregular shapes and multiple islets still attached to the samples. Higher magnification SEM suggests that such islets are related to the presence of flaws, such as lacks of fusion (arrow in Fig. 12a).

Fracture surface morphology indicates two distinct types of spalling behaviour, either “intrapool”, where cracks propagate within the melt pools, or “interpool”, where cracks clearly follow melt pool boundaries. Indeed, the higher concentration of flaws such as lacks of fusion, pores or inclusions at these boundaries, as well as a high gradient of microstructure in this zone [6,7], probably provide preferential sites for voids/cracks nucleation. In samples loaded normally to the Z direction (Fig. 3b), the plane of maximum tension (spall plane) seldom coincides with melt pool boundaries, so that fracture is almost fully intrapool (Fig. 12), with cracks that might follow grains orientations (as suggested in Fig. 12b). In contrast, in samples loaded along the building direction (Fig. 3a), interpool fracture dominates. Because melt pools are dissymmetric (Fig. 1), results depend on the orientation. Upon shock loading along –Z (opposite to the stacking axis), fracture in the spall crater is almost fully interpool, resulting in smooth, convex surfaces

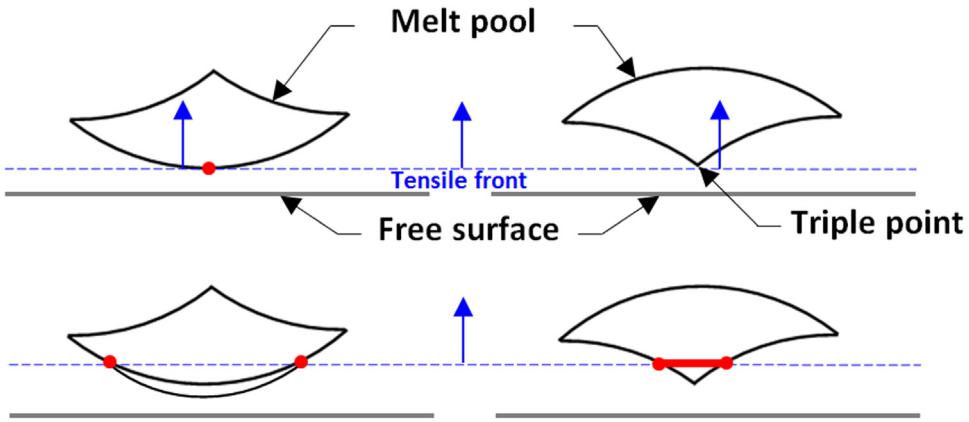


**Fig. 14.** Schematic description of the interaction between the tensile front propagating upwards from the free surface (blue dotted line) and the melt pool boundaries, after shock loading along –Z (left) or +Z (right), at two successive instants (top then bottom).

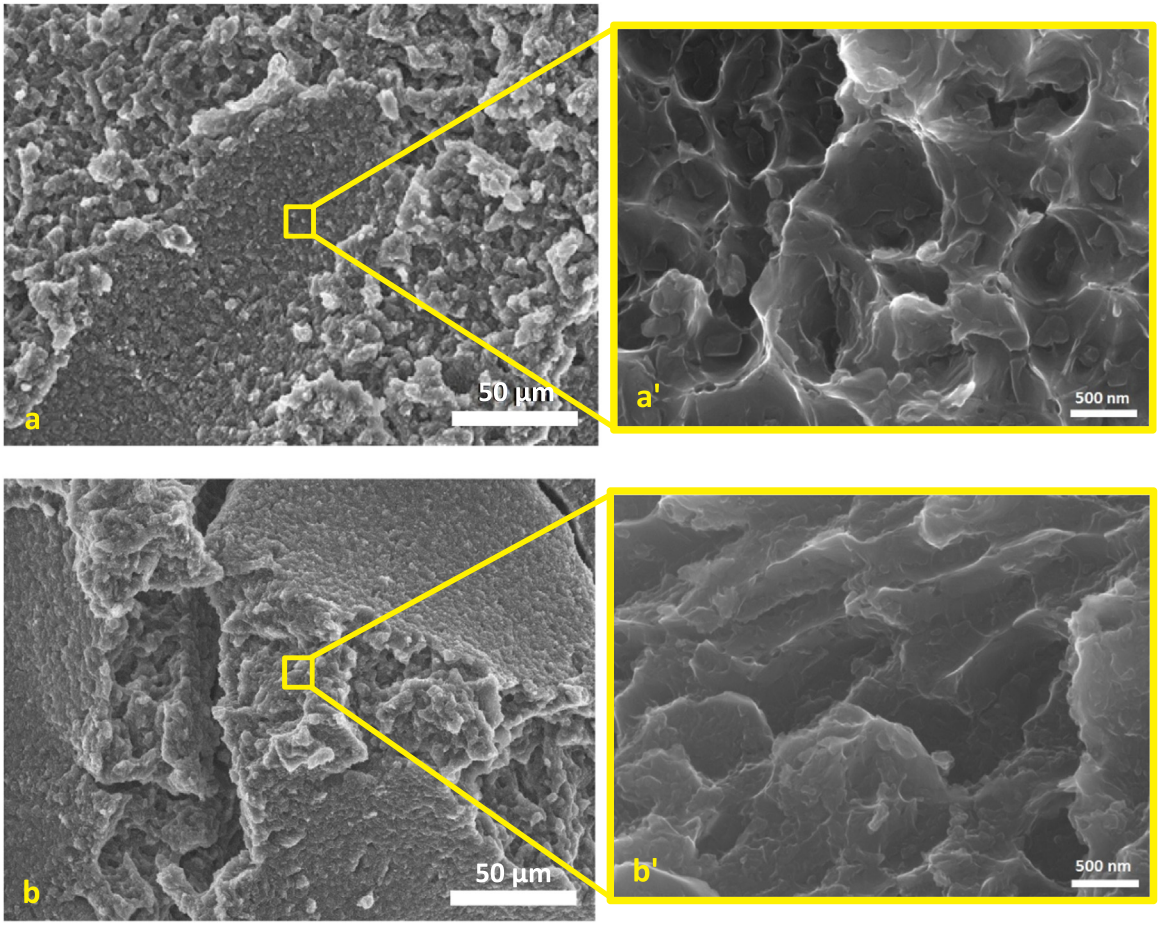


**Fig. 15.** SEM-FEG images of P1-Z-500–2 fracture surface in interpool (a, a′) and intrapool (b, b′) regions.

corresponding to the bottom of the melt pools (Fig. 9), while a combination of both modes is observed after shock loading along +Z (Fig. 10, where intrapool damage is pointed in red and interpool in yellow). This dependence on orientation can be explained by the melt pool geometry ahead of the tensile front (Fig. 14). After a laser shock along -Z, when this front reflecting from the free surface meets the convex surface of the melt pool, fracture starts at these weak frontiers. As they are almost collinear with the tensile front, spallation propagates along these surfaces, relaxing tensile stresses. In the reverse configuration whereby specimens are loaded along +Z, the tensile front first meets the triple point where damage initiation is more difficult because of the local microstructure and the broader angles with the melt pools boundaries. Thus, spallation only starts beyond this point, in the form of intrapool fracture. Next, the decreasing angle formed between the melt pool boundaries and the tensile front becomes favourable to crack propagation, so that additional interpool fracture occurs, leading to the separation of the rest of the melt pool and leaving a smooth concave surface in the crater (Figs. 10 and 11).

The interpool fracture mode leaves clear traces of the melt pools, either concave or convex as discussed above, in the spall crater. These traces include different orientation angles related to the stacking strategy, either 0–67–134° in P1 samples (Figs. 9 and 10) or 0–90° in P2 samples (Fig. 11). Although such different orientations might coexist in one XY section (Fig. 1), they also result from multiple spall at increasing depths beneath the free surface (see Figs. 9b and 11b). Indeed, the reflection of a triangular pressure pulse can produce such multiple spall [28], as stress relaxation accompanying an early fracture may not prevent a later, deeper one due to further tension. Another evidence of such successive spall fractures is illustrated in Fig. 10c, where secondary (interpool) cracks are observed locally deep below the main crater. Finally, the spall craters after shock loading along the Z direction show a peripheral ring (Fig. 9a, Fig. 10a) where damage is mainly intrapool, compared to the centre showing mainly interpool fracture. Cross sections of these crater edges (Fig. 13) clearly show that both regions correspond to two different spall planes at increasing distance from the free surface. Thus, a first spalled layer was formed through intrapool fracture, about 50 µm-deep beneath the free surface. Then, further tension produced secondary spallation at deeper melt pools boundaries, except in the peripheral ring, due to additional relaxation by lateral release waves.

This process of multiple spall partially accounts for the similar spall strength values recorded under both loading directions (Table 4). Indeed, the first fracture to occur is the closest to the free surface, typically 50 µm deep below that surface in our test conditions, where the tensile front has not met favourable melt pool boundaries yet, even in the case of shock loading along the Z direction. Therefore, this first fracture is likely to be mainly intrapool, regardless of the direction of shock application. Because the spall strength inferred from the free surface velocity is related to the relaxation provided only by this first fracture, it is logically found to be independent on the loading direction.

Finally, higher magnification images of the fracture surface in sample P1-Z-500–2 shocked along the +Z axis reveal small ductile dimples in both interpool and intrapool damage types (Fig. 15), with slightly more elongated dimples in intrapool regions. Thus, spall fracture involves the nucleation, growth and coalescence of microvoids in both cases. This indication that both intrapool and interpool spalling processes result from the same ductile behaviour is another possible cause for the fact that the spall strength does not significantly depend on loading directions (Table 4). The small dimple size (sub-µm-order)

suggests that damage nucleation might occur along the denditric network, as Tradowsky et al. showed in their study of tensile properties of AlSi10Mg obtained by SLM [29]. On the other hand, our observations do not seem to corroborate the transition from a ductile to a brittle fracture behaviour reported at high strain rate in impact-loaded AlSi10Mg obtained by SLM [10]. This may be due to the higher shock-induced heating in our case of higher loading pressures. From the peak free surface velocity of about 900 m/s, using Hugoniot data of Al, assumed to provide rough estimations for AlSi10Mg, shock breakout pressure can be evaluated as about 7 GPa, which would correspond to a temperature increase of about 70 K [30]. However, stronger heating can be expected inside the sample before shock pressure decay during propagation up to the free surface. Such temperature rise, although moderate, might partially inhibit the transition mentioned above, but more work is needed to clarify this issue.

## 5. Conclusion

Thin specimens of SLM-produced AlSi10Mg alloys were subjected to laser-driven shocks to investigate their mechanical response at extremely high strain rates. Experiments were performed on two different materials associated with two distinct sets of building parameters, leading to different values of sound speed and initial porosity. Both the yield strength (Hugoniot elastic limit) and spall strength (resistance to high-rate tensile loading) measured in the alloy of higher quality are in very good quantitative agreement with those reported under plate impact loading. Both values are significantly lower in the alloy produced in degraded building conditions. In particular, flaws directly inherited from the SLM process such as lacks of fusion have a significant influence on the decay of the elastic precursor with propagation distance and on the fracture behaviour, leading to spall craters of irregular contours and surfaces. Although the spall strength is found to be roughly independent on loading orientation with respect to building direction (like reported under plate impacts), this orientation is shown to affect drastically the fracture surface morphology, due to the major role of the melt pool boundaries in the initiation and development of spall damage, leading to a combination of “interpool” and “intrapool” fracture modes. However, at a microscopic scale, both modes seem to result from a ductile behaviour involving the nucleation, growth and coalescence of voids leaving dimples in the fracture surface. Thus, the ductile-to-brittle transition reported under plate impacts was not observed under laser shock loading, possibly because of greater shock-induced heating in our experimental conditions.

## Acknowledgements

The authors thank Cyril Dupuytrent and the Thales Group for supporting and funding this work (grant no. 2017/32 V2/CDA136963), as well as Zodiac Aerospace for providing the materials. The authors also gratefully acknowledge everyone within Laboratoire pour l’Utilisation des Lasers Intenses and Institut Pprime, Département Physique et Mécanique des Matériaux, équipe Endommagement et Durabilité who contributed to these experiments.

## Data availability

The raw/processed data required to reproduce these findings cannot be shared at this time as the data also form part of an ongoing study.

## References

[1] W.E. Frazier, Metal additive manufacturing: a review, J. Mater. Eng. Perform. 23 (2014) 1917–1928, https://doi.org/10.1007/s11665-014-0958-z.
[2] J. Gardan, Additive manufacturing technologies: state of the art and trends, Int. J. Prod. Res. 54 (10) (2016) 3118–3132, https://doi.org/10.1080/00207543.2015.1115909.
[3] M.B. Mawale, A.M. Kuthe, S.W. Dahake, Additive layered manufacturing: state-of-the-art applications in product innovation, Concurr. Eng.: Res. Appl. 24 (1) (2016) 94–102, https://doi.org/10.1177/1063293×15613111.
[4] F. Trevisan, F. Calignano, M. Lorusso, J. Pakkanen, A. Aversa, E.P. Ambrosio, M. Lombardi, P. Fino, D. Manfredi, On the Selective laser melting (SLM) of the AlSi10Mg alloy: process, microstructure, and mechanical properties, Mater. (Basel) 10 (1) (2017), https://doi.org/10.3390/ma10010076.
[5] M. Tang, Inclusions, porosity and fatigue of AlSi10Mg parts produced by Selective laser melting, Carne. Mellon Univ. Pittsburgh (Dr. Diss.) (2017).
[6] E. Fella, Selective laser beam melting of AlSi10Mg alloy, Polytecnico Milano (Dr. Diss.) (2016).
[7] M. Godino Martinez, AlSi10Mg parts produced by Selective laser melting (SLM), Univ. Carlos III Madr. KU Leuven (Dr. Diss.) (2013).
[8] K. Kempen, L. Thijs, J. Van Humbeeck, J.-P. Kruth, Mechanical properties of AlSi10Mg produced by selective laser melting, Phys. Procedia 39 (2012) 439–446, https://doi.org/10.1016/j.phpro.2012.10.059.
[9] H. Asgari, A. Odeshi, K. Hosseinkhani, M. Mohammadi, On dynamic mechanical behavior of additively manufactured AlSi10Mg_200C, Mater. Lett. 211 (2018) 187–190, https://doi.org/10.1016/j.matlet.2017.10.001.
[10] E. Zaretsky, A. Stern, N. Frage, Dynamic response of AlSi10Mg alloy fabricated by selective laser melting, Mater. Sci. Eng.: A 688 (2017) 364–370, https://doi.org/10.1016/j.msea.2017.02.004.
[11] T. de Rességuier, S. Hemery, E. Lescoute, P. Villechaise, G.I. Kanel, S.V. Razorenov, Spall fracture and twinning in laser shock-loaded single-crystal magnesium, J. Appl. Phys. 121 (16) (2017) 165104, https://doi.org/10.1063/1.4982352.
[12] D. Koutny, D. Palousek, L. Pantelejev, C. Hoeller, R. Pichler, R. Tesicky, J. Kaiser, Influence of scanning strategies on processing of aluminum alloy EN AW 2618 using Selective laser melting, Mater. (Basel) 11 (2018) 298–315, https://doi.org/10.3390/ma11020298.
[13] J.N. Domfang Ngnekou, Y. Nadot, G. Henaff, J. Nicolai, W. Hao Kan, J.M. Cairney, L. Ridosz, Fatigue properties of AlSi10Mg produced by Additive Layer Manufacturing, Int. J. Fatigue 119 (2019) 160–172, https://doi.org/10.1016/j.ijfatigue.2018.09.029.
[14] J.N. Domfang Ngnekou, Y. Nadot, G. Henaff, J. Nicolai, L. Ridosz, Influence of defect size on the fatigue resistance of AlSi10Mg alloy elaborated by selective laser melting (SLM), Procedia Struct. Integr. 7 (2017) 75–83, https://doi.org/10.1016/j.prostr.2017.11.063.
[15] N.T. Aboulkhair, N.M. Everitt, I. Ashcroft, C. Tuck, Reducing porosity in AlSi10Mg parts processed by selective laser melting, Addit. Manuf. 1–4 (2014) 77–86, https://doi.org/10.1016/j.addma.2014.08.001.
[16] J. Stef, A. Poulon-Quintin, A. Redjaimia, J. Ghanbaja, O. Ferry, M. De Sousa, M. Gouné, Mechanism of porosity formation and influence on mechanical properties in selective laser melting of Ti-6Al-4V parts, Mater. Des. 156 (2018) 480–493, https://doi.org/10.1016/j.matdes.2018.06.049.
[17] D. Xiao, Q. Fan, C. Xu, X. Zhang, Measurement methods of ultrasonic transducer sensitivity, Ultrasonics 68 (2016) 150–154, https://doi.org/10.1016/j.ultras.2016.02.017.
[18] L.M. Barker, R.E. Hollenbach, Laser interferometer for measuring high velocities of any reflecting surface, J. Appl. Phys. 43 (1972) 4669, https://doi.org/10.1063/1.1660986.
[19] W.F. Hemsing, Velocity sensing interferometer (VISAR) modification, Rev. Sci. Instrum. 50 (1979) 73–78, https://doi.org/10.1063/1.1135672.
[20] L.M. Barker, The accuracy of VISAR instrumentation, shock compression of condensed matter, AIP Conf. Proc. 429 (1998) 833–836, https://doi.org/10.1063/1.55598.
[21] T. de Rességuier, H. He, P. Berterretche, Use of laser-accelerated foils for impact study of dynamic material behaviour, Int. J. Impact Eng. 31 (8) (2005) 945–956, https://doi.org/10.1016/j.ijimpeng.2004.07.003.
[22] L. Berthe, R. Fabbro, P. Peyre, L. Tollier, E. Bartnicki, Shock waves from a water-confined laser-generated plasma, J. Appl. Phys. 82 (6) (1997) 2826–2832, https://doi.org/10.1063/1.366113.
[23] T. Antoun, L. Seaman, D.R. Curran, G.I. Kanel, S.V. Razorenov, A.V. Utkin, Spall Fracture, Springer, New York, 2002.
[24] J.P. Billingsley, The decay of the Hugoniot Elastic Limit, Int. J. Im. Eng. 21 (4) (1998) 267–281, https://doi.org/10.1063/1.55482.
[25] G.T. Gray III, C.M. Knapp, D.R. Jones, V. Livescu, S. Fensin, B.M. Morrow, C.P. Trujillo, D.T. Martinez, J.A. Valdez, Structure/property characterization of spallation in wrought and additively manufactured tantalum, AIP Conf. Proc. 1979 (2018) 1, https://doi.org/10.1063/1.5044799 〈DOI:〉.
[26] B. Glam, S. Eliezer, D. Moreno, L. Perelmutter, M. Sudai, D. Eliezer, Dynamic fracture and spall in aluminum with helium bubbles, Int. J. Fract. 163 (2010) 217–224, https://doi.org/10.1007/s10704-009-9437−1.
[27] Y. Wang, M. Qi, H. He, L. Wang, Spall failure of aluminum materials with different microstructures, Mech. Mater. 69 (1) (2014) 270–279, https://doi.org/10.1016/j.mechmat.2013.11.005.
[28] J.S. Rinehart, Scabbing of metals under explosive attack: multiple scabbing, J. Appl. Phys. 23 (1952) 1229–1233.
[29] U. Tradowsky, J. White, R.M. Ward, N. Read, W. Reimer, M.M. Attallah, Selective laser melting of AlSi10Mg: Influence of post-processing on the microstructural and tensile properties development, Mater. Des. 105 (2016) 212–222, https://doi.org/10.1016/j.matdes.2016.05.066.
[30] R. Kinslow, High-Velocity Impact Phenomena, Academic Press, 1970, pp. 530–568.